

**Deleted:** This is a non-peer reviewed preprint submitted to EarthArXiv, subsequent versions of this manuscript may have slightly different content. [i](#)

# Quantifying mantle mixing through configurational Entropy

Erik van der Wiel<sup>1</sup>, Cedric Thieulot<sup>1</sup>, Douwe J.J. van Hinsbergen<sup>1</sup>

<sup>1</sup> Department of Earth Sciences, Utrecht University, Princetonlaan 8A, 3584 CB Utrecht, the Netherlands

Corresponding author: [e.vanderwiel@uu.nl](mailto:e.vanderwiel@uu.nl)

## 1 Abstract

2 Geodynamic models of mantle convection provide a powerful tool to obtain insights  
3 into the structure and composition of the Earth's mantle that resulted from a long history of  
4 differentiating and mixing. Comparing such models with geophysical and geochemical  
5 observations is challenging as these datasets often sample entirely different temporal and  
6 spatial scales. Here, we explore the use of configurational entropy, based on tracer and  
7 compositional distribution on a global and local scale. We show means to calculate  
8 configurational entropy in a 2D annulus and find that these calculations may be used to  
9 quantitatively compare long-term geodynamic models with each other. The entropy may be  
10 used to analyze, with a single measure, the mixed state of the mantle as a whole and may  
11 also be useful to compare numerical models with local anomalies in the mantle that may be  
12 inferred from seismological or geochemical observations.

Deleted: validate

Deleted: against

## 14 1. Introduction

15 Mantle convection models that are used to simulate the evolution and dynamics of  
16 the solid Earth are built on different sets of observations each providing their own  
17 constraints to validate the state of the mantle through time (e.g., (Dannberg & Gassmöller,  
18 2018; Gerya, 2014). For instance, with the advent of full-plate kinematic reconstructions of  
19 the past 100s Ma (e.g., (Domeier & Torsvik, 2014; Merdith et al., 2021), mantle models can  
20 now be driven by plate motions through geological time (e.g., (Coltice & Shephard, 2018;  
21 Flament et al., 2022; Heister et al., 2017). Such experiments then lead to a prediction of the  
22 structure and composition of the mantle that may be compared to geological, geochemical,

Deleted: stooled

26 or seismological observations from the modern Earth (e.g. (Bower et al., 2015; Flament et  
27 al., 2022; Li et al., 2023; Lin et al., 2022; Yan et al., 2020).

28 Key observables of the modern Earth that may be predicted by models are anomalies  
29 in mantle structure or composition that result from mantle mixing, or absence thereof. For  
30 instance, seismic tomography provides images of the present-day mantle as relative slow  
31 and fast regions in terms of seismic wave propagation, which can relate to variations in  
32 temperature and/or composition such as slabs or mantle plumes (Koelemeijer et al., 2017;  
33 Ritsema & Lekić, 2020). The heterogeneity of the Earth's mantle is also reflected in  
34 geochemical observations of magmatic rocks, oceanic island basalts (OIB) and mid-oceanic  
35 ridge basalt (MORB), which suggest the existence of depleted, enriched, and even primordial  
36 mantle reservoirs, i.e. unmixed regions that maintain a geochemically distinct composition  
37 (Jackson et al., 2018; Jackson & Macdonald, 2022; McNamara, 2019; Stracke et al., 2019).

38 Notably, seismological and geochemical heterogeneities may entirely, partly, or hardly  
39 overlap, and observations may relate to spatial and temporal scales. Seismology reveals  
40 seismic velocity anomalies in the mantle on scales of 100s to 1000s of km, varying from slabs  
41 to LLSVPs (e.g., (Garnero et al., 2016; Ritsema et al., 2011; van der Meer et al., 2018).

42 Geochemical differences between MORBs from the Atlantic, Pacific and Indian Ocean  
43 indicate compositional heterogeneity on a hemispheric scale (Doucet et al., 2020; Dupré &  
44 Allègre, 1983; Hart, 1984; Jackson & Macdonald, 2022), geochemical zonation within a single  
45 plume system is evidence for heterogeneities on a 100 km scale (Gazel et al., 2018; Hoernle  
46 et al., 2000; Homrighausen et al., 2023; Weis et al., 2011), whereas micro-scale analysis  
47 reveals even major variations between samples (Stracke et al., 2019). All such variations may  
48 result from a cycle of geochemical differentiation and renewed mixing that is associated with  
49 mantle convection and that eventually may be predicted by mantle convection models. To

Deleted: entirely

51 this end it is important to also able to define or quantify the mixed state of the modern  
52 mantle from a suitable numerical mantle convection model on the relevant range of spatial  
53 scales. While mixing technically involves diffusion at small scales and the term stirring has  
54 been proposed to account for the mechanical stretching and folding (Farnetani & Samuel,  
55 2003), which is infact our interest here, we shall nevertheless use the term mixing in the  
56 remainder of the manuscript as we use varying 'compositions' that are able to mix.

Deleted: be

57 It has long been recognized that mantle convection is complex, and its mixing has  
58 been studied for decades, see (Kellogg, 1993; van Keken et al., 2003) for early reviews on  
59 this topic. Unsurprisingly, the advent of high-performance numerical modelling in the mid-  
60 90's saw a resurgence in the characterization of mantle mixing and its quantification. Various  
61 approaches have been proposed over the years, but the vast majority of these are based on  
62 the time evolution of a swarm of particles. Early studies (such as (Hoffman & McKenzie,  
63 1985; Olson et al., 1984a, 1984b; Richter et al., 1982; Schmalzl et al., 1996)) use statistics to  
64 arrive at a mixing time scale. Another approach using the presence, addition, and/or  
65 removal of particles in a modelled domain is used to quantify mixing-times and degassing  
66 (sampling of primitive mantle) (Gottschaldt et al., 2006; Gurnis & Davies, 1986a, 1986b), to  
67 measure strain and the dispersal of tracers (Christensen, 1989; Kellogg & Turcotte, 1990) or  
68 to study the development of time-dependent mantle-heterogeneities (Hunt & Kellogg,  
69 2001). Note that other methods have been proposed, such as a line method (Ten et al.,  
70 1998), a correlation dimension method (Stegman et al., 2002) and a hyperbolic persistence  
71 time method (Farnetani & Samuel, 2003).

Deleted:

72 More recently another approach has dominated the mantle mixing literature: it  
73 consists in measuring the Lyapunov time, which is the characteristic timescale for which a  
74 dynamical system is chaotic, or rather its inverse the Lyapunov exponent. It can be shown



77 that mixing is laminar or turbulent by evaluating the Lyapunov exponent, the larger the  
78 exponent the more efficient the mixing is. A typical example uses a steady state velocity  
79 pattern obtained in a 3D spherical domain to advect passive particles (van Keken & Zhong,  
80 1999). They use a very common approximation to the Lyapunov exponent, i.e., the Finite  
81 Time Lyapunov Exponent, which is based on the evaluation of the distance between a  
82 multitude of particle pairs that are initially very close to each other (i.e., stretching of this  
83 original distance after 4 Ga). This shows a strong diversity in mixing behavior dependent on  
84 the mantle flow characteristics. Other studies that used the same approach in studying a  
85 variety of mantle convection problems include (Bello et al., 2014; Bocher et al., 2016; Colli et  
86 al., 2015; Coltice, 2005; Coltice & Schmalzl, 2006; Farnetani et al., 2002; Farnetani & Samuel,  
87 2003; Ferrachat & Ricard, 1998, 2001; Samuel et al., 2011; Tackley & Xie, 2002; Thomas et  
88 al., 2024).

89 In this study, we investigate the merits of yet another approach, the configurational  
90 (or 'Shannon') entropy for quantifying compositional mixing of particles through flow on a  
91 global or local scale (Shannon, 1948). Despite its popularity in other fields it has only  
92 minimally been used in geosciences (e.g., (Camesasca et al., 2006; Naliboff & Kellogg, 2007).

93 We develop the application of configurational entropy to the 2D cylindrical mantle  
94 convection models which we recently developed (van der Wiel et al., 2024), implementing  
95 measures for local and global entropy of mixing that incorporates information on  
96 composition. We aim to use configurational entropy to quantify the degree of mixing on  
97 different scales for different hypothetical initial compositional configurations of the mantle  
98 and evolution thereof over time. Subsequently, we discuss how configurational entropy may  
99 be used as a bridge for quantitative comparison between mantle convection models and  
100 geological, seismological, or geochemical observations.

Deleted: ¶  
→ Here,

Formatted: Indent: First line: 1.27 cm

Deleted: (van der Wiel et al., 2023)

## 104 2. Methods

### 105 2.1. Mixing entropy

106 Configurational entropy is analogous to the Shannon entropy (Shannon, 1948) and  
107 related to the probabilities derived from the distribution of particles with a certain value,  
108 i.e., composition. It can be used to track the mixing of particles independently of the  
109 physical process causing that mixing in numerical simulations as well as laboratory  
110 experiments. This entropy is widely used and has a large variety of applications, including  
111 fluid or magma mixing (Camesasca et al., 2006; Naliboff & Kellogg, 2007; Perugini et al.,  
112 2015), transport of plastic in oceans (Wichmann et al., 2019), distribution of seismicity in  
113 earthquake populations (Goltz & Böse, 2002), or the quantification of uncertainty in  
114 geological models (Wellmann & Regenauer-Lieb, 2012).

115 The definition of the configurational entropy  $S$  is based on the proportion of a  
116 specific distribution of particles in a domain tessellated by non-overlapping cells. For this we  
117 use passive particles, or tracers, that are advected in a flow model leading to particle  
118 trajectories. The entropy depends on the distribution of particles, the number of cells and  
119 the initial compositional distribution (see section 2.3). Let  $C$  be the number of compositions  
120 and  $M$  the number of cells in the domain. The entropy is calculated based on the discretized  
121 particle density  $\rho_{c,j}$  (Eq. 1), i.e., the amount of particles of composition  $c$  in cell  $j$ ,

$$122 \rho_{c,j} = \frac{n_{c,j}}{N_c} \quad (1)$$

123 where  $N_c$  is the total number of  $c$ -particles divided by the number of cells  $M$ . This assumes  
124 that cells are of equal area, which will be used here in our 2D application. Hence,  $N_c$  is the  
125 same for all cells. From the compositional density  $\rho_{c,j}$  we calculate  $P_{j,c}$  which is the  
126 proportion of particles of composition  $c$  in cell  $j$  relative to the total number of particles in

Deleted: E

Deleted:

Deleted: describes how fast information on compositional particle distribution is lost through flow

Deleted:

Deleted: It

Deleted: probability

Deleted: distribution

Deleted: the conditional probability

136 the cell, both measured in terms of density through Eq. (2). We calculate  $P_j$  through the cell-  
 137 sum of all compositional densities in Eq. (3).  $P_j$  is the proportion of the amount of particles  
 138 in a cell relative to all the particles in the system. The quantities we describe here as  
 139 proportions would be considered probabilities, or conditional probabilities, in statistical  
 140 physics.

$$141 \quad P_{j,c} = \frac{\rho_{c,j}}{\sum_{c=1}^C \rho_{c,j}} \quad (2)$$

$$142 \quad P_j = \frac{\sum_{c=1}^C \rho_{c,j}}{\sum_{j=1}^M \sum_{c=1}^C \rho_{c,j}} \quad (3)$$

143 Next, Eq. 4 defines the global entropy  $S_{pd}$  of the particle distribution.

$$144 \quad S_{pd} = -\sum_{j=1}^M P_j \ln P_j \quad (4)$$

145 which quantifies the global spatial heterogeneity of the particle distribution independent of  
 146 composition (Naliboff & Kellogg, 2007). At the cell level, the local entropy  $S_j$  for cell  $j$  can be  
 147 defined for the mixture of particles with different compositions:

$$148 \quad S_j = -\sum_{c=1}^C P_{j,c} \ln P_{j,c} \quad (5)$$

149 Finally, the global entropy  $S$  of the particle distribution, accounting for composition, is the  
 150 weighted average of  $P_j$  (Eq. 3) and the local entropy  $S_j$  (Eq. 4) through Eq. (6) (Camesasca et  
 151 al., 2006).

$$152 \quad S = \sum_{j=1}^M P_j S_j \quad (6)$$

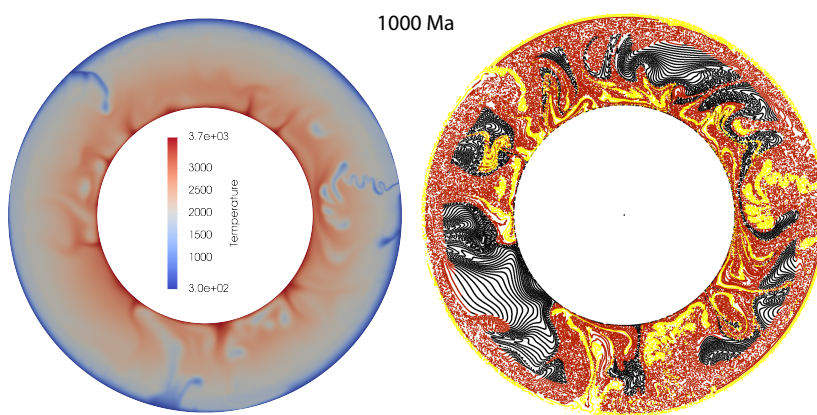
153 Maximum entropy is achieved when all particle densities  $\rho_{c,j}$  are equal, i.e., the  
 154 distribution of composition and number of particles are the same in each cell. Each entropy  
 155 above has a different maximum which depends on either the number of cells for ( $S_{pd}$ ) or the  
 156 number of compositions used (for  $S$  and  $S_j$ ). To compare entropies between mixing models  
 157 with different initial conditions, we normalize the entropies by dividing each by its  
 158 maximum. The maximum for  $S_{pd}$  is equal to  $\ln M$ , while for  $S_j$  and  $S$  the maximum is  $\ln C$

Deleted: for finding a group of particles of composition  $c$  in cell  $j$ ...

Deleted: ¶ and as well the probability for the cell-sum of compositional densities  $P_j$  by Eq. (3),

Formatted: Indent: First line: 1.27 cm

164 (Camesasca et al., 2006). This provides values for all entropies between the endmembers 0  
 165 (entirely segregated composition) and 1 (uniformly mixed). The maximum value for  $S_{pd}$  can  
 166 only be reached when all compositions are present in equal ratios. Entropy calculations of  
 167 four simple educational examples are shown and explained in appendix A to help the reader  
 168 appraise these quantities.



169  
 170 *Figure 1 - Snapshot from model R at t=1000 Ma showing the temperature field in Kelvin (left) and passive particles colored*  
 171 *by composition (lithosphere: yellow, upper mantle: red, lower mantle: black).*

## 172 2.2 Mantle convection model

173 We apply the configurational entropy to the quantification of mixing in a recently  
 174 developed 2D numerical mantle model in a 2D cylindrical geometry that simulates 1000 Ma  
 175 of ongoing mantle convection and subduction (van der Wiel et al., 2024). The convection  
 176 model was designed to evaluate the sensitivity of inferred lower mantle slab sinking rates  
 177 (van der Meer et al., 2018) to the vigor of mantle convection. The simulations comprised  
 178 dynamically self-consistent one-sided subduction below freely moving, initially imposed,  
 179 continents at the surface, culminating in slab detachment followed by sinking of slab  
 180 remnants across the lower mantle (Fig. 1). The surface velocity in the model were generally  
 181 between 1 and 4 cm/a, which may be compared to the reconstructed values of 4 cm/a of

Deleted: (van der Wiel et al., 2023)

183 ~~Zahirovic et al., (2015) and the obtained~~ average slab sinking rates ~~were~~ in the range of  
184 those that were inferred from correlations between the location of imaged lower mantle  
185 slabs and their geological age (van der Meer et al., 2018). This modelling qualitatively  
186 illustrated the degree of mixing in a modelled mantle and the potential preservation of an  
187 unmixed ~~original mantle~~, advected ~~slabs~~, or (partly) homogenized, mixed mantle shown by  
188 the distribution of particles.

**Deleted:** Model plate motions were in the range of reconstructed values (Zahirovic et al., 2015) and

**Deleted:** could be obtained

189 We quantify the degree of mantle mixing in the model by investigating the local and  
190 global mixing entropies (Section 2.1) for model *R* of van der Wiel et al. (2023) at different  
191 resolutions. We also illustrate how mixing entropy quantifies the mixing of a different model  
192 (model *P*) that showed significantly higher slab sinking rates than inferred for the lower  
193 mantle and that displayed a higher degree of mantle mixing (van der Wiel et al., 2023). For  
194 this purpose, we only used the passive particle distribution available from the models in van  
195 der Wiel et al., 2023. The cells used to calculate the configurational entropy (see section 2.4)  
196 are independently substantiated and therefore not the same as used in the numerical  
197 model, for any additional information of these models we refer the reader to van der Wiel et  
198 al., 2023.

**Deleted:** primordial

**Deleted:** unmixed

**Deleted:** (e.g., subducted)

## 200 2.3 Initial composition

201 To illustrate how we track compositional evolution with configurational entropy, we  
202 assign a compositional distribution to our example models with two different approaches. In  
203 case A, we assign a compositional distribution in the initial model, and each tracer will keep  
204 its initial composition through time. We divide the annulus in two concentric parts at a  
205 radius of 5100 km and assign the inner and outer part a different composition (simply put: a  
206 different color). This creates a 50-50 ratio between the number of particles of each

composition. Case B uses dynamic compositions, i.e., the composition of a particle may change over time. We use three compositions whose relative ratios are allowed to change over time depending on the particle's depth in the model. Initially, we define particles as lower mantle when they start below 660 km depth in the model, upper mantle if they start between 100 and 660 km, and lithosphere if between 0 and 100 km depth. Particles keep their 'lower mantle' composition as long as they do not ascend above the 660 km during model evolution. Any particle that moves from a deeper reservoir into a shallower one will see its composition changed to the shallower reservoir and will maintain this composition for the remainder of model time. This approach is an example that may be used in a study to characterize the secular geochemical differentiation of the solid Earth.

223

#### 2.4 Cell distribution

Entropy as calculated in this study also depends on the number and distribution of cells, which is independent of the mesh used in the numerical model itself. To ensure an approximately equal cell-area throughout our domain, we vary the number of cells per radial layer. The cell-area is determined by the product of the radial extent  $\delta r$  and lateral extent  $\delta \theta$  that follows from the number of radial layers and the number of cells along the core-mantle-boundary (CMB) circumference. Varying cell-area may be important to compare the outcome of a numerical model with datasets that have very different resolutions (e.g., seismology versus geochemistry). We illustrate different cell resolutions with our 2D example model, but a similar approach may be used for a 3D model albeit with a different tessellation (Thieulot, 2018). One should note that in this set-up our cells are chosen to be of equal area while in a 3D model this should be equal volume.

236 The lowest resolution (10x40) contains 40 cells along the CMB, increasing across the  
 237 10 layers to 68 cells along the surface, for a global total of 539 cells (Fig. 2). The highest  
 238 resolution that we illustrate (20x160) then gives a global total of 4430 cells (Fig. 2). The  
 239 numerator  $\rho_{c,j}$  for the proportion calculations (Eqs 2 & 3) for cells that do not contain a  
 240 particle ( $\sum_{c=1}^C \rho_{c,j} = 0$ ) would cause a problem in its contribution to the entropy via the  
 241 natural logarithm. Note that  $\lim_{x \rightarrow 0} x \ln x = 0$  and that therefore cells without a particle do not  
 242 add to any of the entropies, these cells are skipped in practice in the summation of Eqs (4-6).

Deleted: probability

Deleted: contribute to

### 244 3. Results

245 In this section, we describe the various obtained entropies. Starting with the particle  
 246 distribution  $S_{pd}$ . Next, we underline the importance of resolution for the local entropy  $S_j$  in  
 247 our example model at different resolutions for the static composition distribution (case A)  
 248 and show how the local entropy evolves over time. Finally, we show the temporal evolution  
 249 of the global entropy  $S$  for this model, which is also influenced by resolution and  
 250 compositional choices before we elaborate on the use of dynamic compositions (case B,  
 251 section 3.4).

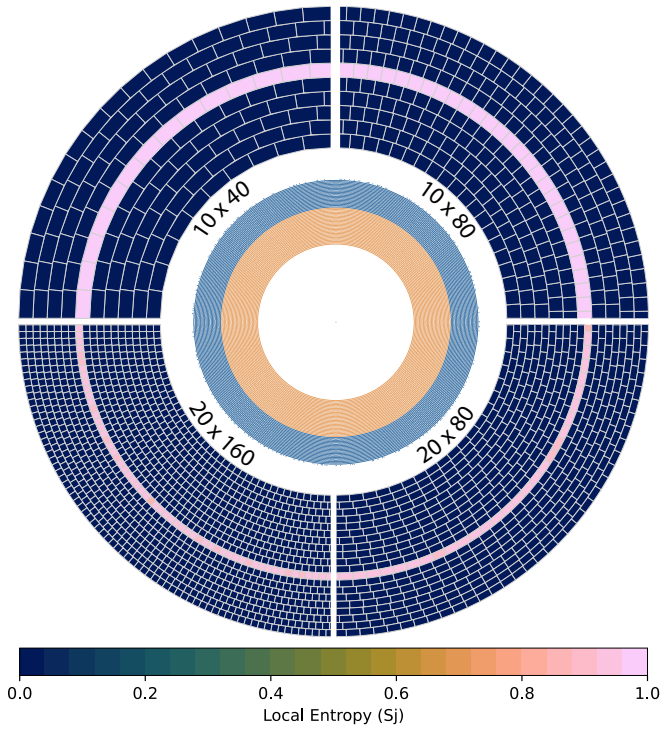


Figure 2: Representation of the various tested resolutions. Shown is the initial ( $t=0$  Ma) particle distribution (inner annulus) and local entropy  $S_j$  (outer annulus) for the static 50/50 composition distribution (case A). The cells with a high  $S_j$  (pink) indicate that both compositions are present, the unmixed cells (blue) contain only one composition.

### 3.1 Global particle distribution ( $S_{pd}$ )

A total of ~96,000 of particles are initially distributed in a regular pattern (Fig. 2), equally spaced throughout the annulus. Over time, these particles are passively advected and their spatial distribution thus changes. The large number of particles in the initial distribution provides a good coverage in all cells as quantified by the normalized global entropy of particle distribution  $S_{pd}$  which is at the modelling start close to 1 for both cases A & B at the start (Fig. 3). As the initial composition ratios of case B are not equal (about 72% lower mantle, 25% upper mantle, and 3% lithosphere)  $S_{pd}$  is not 1 as for case A, but ~0.95, still indicating that particles are distributed equally.



Over time, as particles are advected, the  $S_{pd}$  does not change significantly for case A in which particles cannot change composition, but it does change for case B (Fig. 3). This is caused by the secular change in composition ratios in case B (Fig. 8 of van der Wiel et al., 2023).  $S_{pd}$  increases due to the increased percentage of lithosphere and upper mantle particles in the domain. We tested the effect of cell resolution on  $S_{pd}$  for both cases, which does not show significant differences (Fig. 3). This indicates that the number of particles used in our calculations is sufficient, also for our highest resolution (20x160).

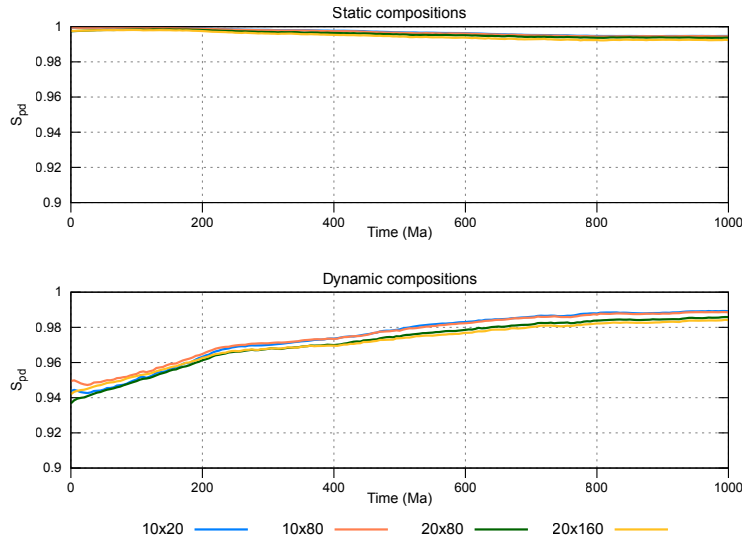


Figure 3: Time evolution of  $S_{pd}$  for the static (case A) and dynamic (case B) composition distributions of the four used resolutions.

### 277 3.2 Local entropy ( $S_j$ )

278 A local entropy of 1 means that the ratio of particle compositions within a cell is  
279 equal to the global composition ratio, e.g. in the initial distribution for case A (Fig. 2).  $S_j = 0$   
280 indicates that all particles in a cell have the same composition, although it does not indicate  
281 which composition. We illustrate the temporal evolution of particle distribution in 250 Ma  
282 steps (Fig. 4) for which we use the static particle composition ratio of case A and a cell  
283 resolution of 10x80 at the CMB (Fig. 3). After 250 Ma of convection evolution the initial  
284 distribution is undisturbed in most parts of the domain. The two compositions are only  
285 displaced since the onset of convection, but barely mixed. Mixing is concentrated around  
286 two major zones of downwelling where a narrow zone of single cells shows a local entropy  
287  $S_j$  that is non-zero (Fig. 4a).

288 At 500 Ma, some of the sharp boundaries between the two compositions have  
289 moved and a mixed boundary zone formed locally, reflected by the broader zone of non-zero  
290 local entropy (Fig. 4b). After 750 Ma, most of the upper mantle (top three cells) has  $S_j > 0$   
291 and zones in the lower mantle are mixed as well (Fig. 4c): the two starting compositions have  
292 been displaced and mixed through the mantle. At the end of the model, at 1000 Ma, the  
293 number of cells with non-zero  $S_j$  in the upper mantle has decreased further, the zones of  
294 fully ( $S_j \approx 1$ ) mixed lower mantle have increased in area. However, there are still zones of  
295 unmixed ( $S_j = 0$ ) composition present. Unmixed initial 'lower' composition is preserved  
296 mainly in the mid-mantle while unmixed initial 'upper' composition is preserved near the  
297 CMB, i.e., this material sunk and was displaced, but did not mix (Fig. 4d).

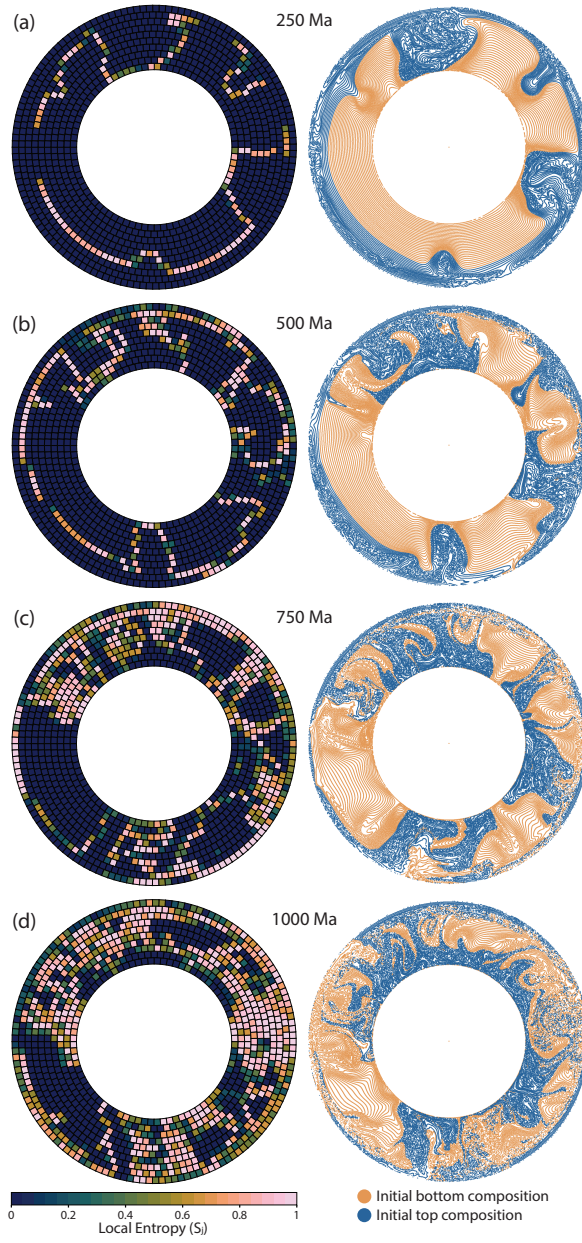


Figure 4 - Local Entropy  $S_j$  (left) and particle distribution (right) at 250 Ma intervals of the model (model R - van der Wiel et al., 2023) with a static 50/50 ratio particle composition (case A) at a resolution of 10x80 cells.

302 Even though cell resolution does not significantly impact  $S_{pd}$  it does affect the local  
303 entropy  $S_j$  (and thus also the global entropy, see next section). A smaller-sized cell mesh will  
304 have fewer particles per cell, which increases the likelihood of sampling particles of only one  
305 composition in zones with limited mixing, leading to zero local entropy. Doubling the angular  
306 resolution from 10x40 to 10x80 shows on a global scale a similar trend after 1000 Ma of  
307 convection: three zones of unmixed (low  $S_j$ ) mantle separated by three zones of mixed  
308 mantle (high  $S_j$ ) (Fig. 5). However, it does show some increased detail in local entropy,  
309 mainly in the ‘mixed’ zones of the model (Fig. 5). The large unmixed zones are of similar size  
310 for these two resolutions, although the ratio of cells with a low  $S_j$  compared to high  $S_j$   
311 changed. The larger unmixed zones are composed of initial ‘lower’ composition (Fig. 4d).

312 A radial increase in resolution, from 10 to 20 cells across the domain, refines the  
313 calculation of local entropy. The number of cells with  $S_j = 0$  becomes larger and increases  
314 the size of the three main unmixed zones. At this resolution,  $S_j$  resolves the ‘continents’:  
315 thicker portions of lithosphere that were initially placed in the model (See Fig 2. of van der  
316 Wiel et al., 2023). The 20x80 resolution has unmixed cells in regions that had high  $S_j$  at  
317 lower resolutions (Fig. 5). Finally, with the 20x160 mesh resolution, zones of initial upper and  
318 lower composition (Fig. 4d) show up as low  $S_j$  bounded by a single line of cells with high  $S_j$   
319 (Fig. 5). At this resolution the local entropy calculation resolves mantle structures such as the  
320 boundaries between slabs and ambient mantle, showing mantle structure mapped into the  
321 local entropy of mixing.

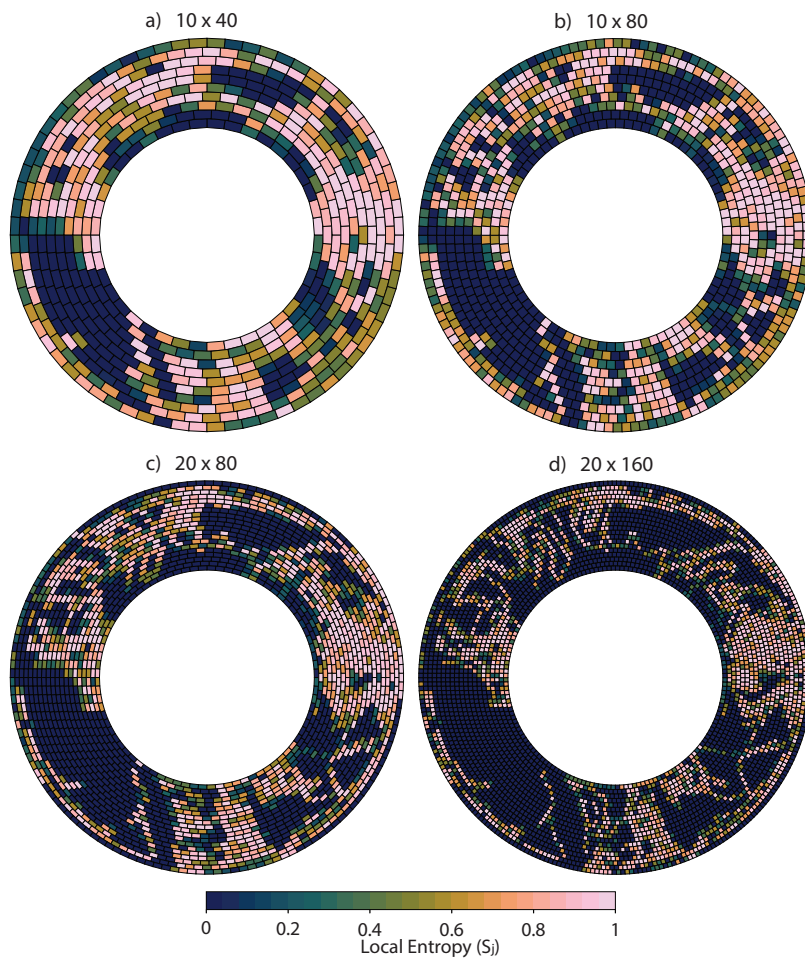


Figure 5 - Local Entropy  $S_i$  after 1000 Ma of mantle convection for the Reference model (van der Wiel et al., 2023) at four different resolutions of cells used to calculate the local entropy where  $b$  is identical as figure 4d.

### 3.3 Global entropy ( $S$ )

The global entropy is a weighted average of the particle distribution proportion  $P_j$  over cells and the compositional distribution within the cells  $S_j$  (Eq. 6). Because the particle distribution irrespective of composition is almost equal to 1 in all tests (Fig. 2, section 3.1), we may consider the entropy  $S$  as proxy for global compositional mixing. For the initial

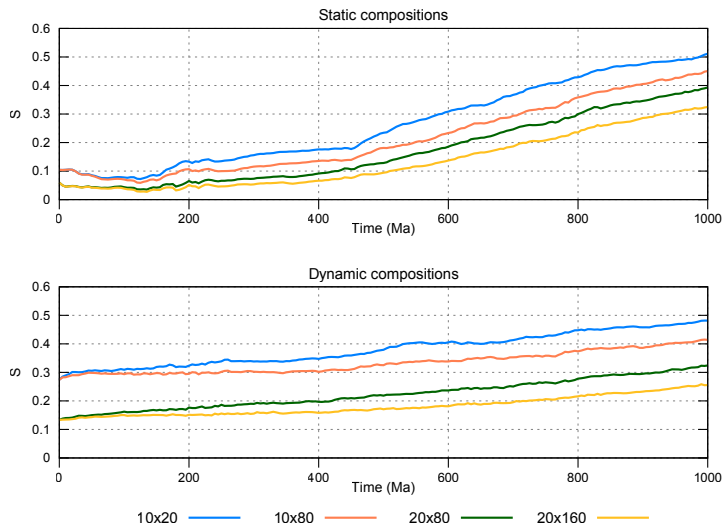
Deleted: probability

331 distribution of composition based on depth, almost all cells have a local entropy  $S_j = 0$ ,  
332 apart from the cells that straddle the compositional boundary (Fig. 2). This distribution is an  
333 unmixed state of the mantle and has a low global entropy,  $S = 0.1$  for the resolutions with  
334 10 radial levels and  $S = 0.06$  for those with 20 radial levels (Fig. 6). The lateral resolution  
335 does not matter for the initial distribution as the ratio of non-zero to zero  $S_j$  cells is the  
336 same.

337 While the mantle flow model evolves, compositions become more mixed and the  
338 global entropy increases depending on mesh resolution, whereby smaller cells have a higher  
339 chance to sample only one composition. Therefore, a higher resolution (smaller cells) yields  
340 a lower global entropy after 1000 Ma of mantle convection: the 20x160 resolution yields  $S =$   
341 0.32 while the 10x40 resolution yields  $S = 0.51$  (Fig. 6).

Deleted: spherical

Deleted: probability



342  
343 Figure 6 - Global Entropy  $S$  of the model through time for different cell resolutions. Top: Case A (static compositions, bottom:  
344 case B (dynamic compositions).

### 3.4 Case study: entropy with dynamic compositions

Case B, which has dynamic compositions that depend on compositional evolution in the model, presents a practical application of the configurational Entropy. We track the entropy as the compositional ratios evolve and mix over time. The total number of particles that have been part of the lithosphere and subducted increases over time as new lithosphere and slab is being created while the volume of material that stays in the lower mantle decreases. In our example model, after 1000 Ma, the initial volumes of 3% lithosphere, 25% upper mantle, and 72% lower mantle have changed to 25% with lithosphere 'composition', 50% upper mantle and 25% lower mantle. In this example, the dynamic composition implies that no lower mantle composition exists above the 660 km-discontinuity and therefore the upper mantle cannot have a local entropy of 1. However, in parts of the lower mantle the three compositions are mixed where high local entropy is present. The parts of the domain containing subducted lithosphere are better mixed, indicative of the convective mixing behavior of our model. With the highest mesh resolution we can resolve the upper- to lower-mantle boundary in the local entropy as well as active and past locations of subduction (Fig. 7a).

The unmixed zones are of particular interest since they may provide direct information about compositions after 1000 Ma of convection. For all compositions there are cells with an unmixed signal, revealing the state of preservation of these compositions over time and over the whole domain. The entropy figures illustrate for instance the survival of unmixed original lower mantle material in the model, the fate of subducted lithosphere, and how upper mantle material is entrained downward during subduction (Fig. 7a).

This case has an entirely different local entropy than the static composition distribution of case A (Fig. 5). The dynamic case mainly focusses on the fate of subducted

Deleted: has

Deleted: 'primordial'

373 lithosphere rather than global mixing of the upper and lower part of the domain. As in the  
374 example with a static composition (case A), the global entropy  $S$  for dynamic compositions is  
375 also cell-size-dependent. The initial global entropy is higher than for static compositions as  
376 there are now two compositional boundaries and over time the entropy only increases up to  
377  $S = 0.25$  for the 20x160 resolution. For the 10x40 resolution,  $S = 0.48$  after 1000 Ma which  
378 is in the same range as the static two-composition example (Fig. 6).

379 Finally, we use the dynamic composition to illustrate how changing the vigor of  
380 mantle convection changes the entropy. To this end, we compute the entropy after 1000 Ma  
381 using a model in which much higher sinking rates of subducted slabs occurred than inferred  
382 (model P - van der Wiel et al., 2023) and that consequently has faster mantle flow. Fig. 7b  
383 illustrates that this model is much more mixed after 1000 Ma of convection than in model R  
384 (Fig. 7a). It has cells with a local entropy close to 1 throughout much of the domain, unmixed  
385 zones are smaller and located only in the top of lower mantle. Most of the local entropies  
386 are in the mid-mixed range. This is because only 10% of the original 'lower mantle'  
387 composition remains. Global entropy  $S$  equals 0.42 for this model at the 20x160 resolution,  
388 and even 0.60 for the 10x40 resolution, significantly higher than the reference model with  
389 dynamic composition (Fig. 6). This example illustrates that the configurational entropy is  
390 able to quantify mixing states in mantle convection models and is sensitive to overall  
391 changes in model behavior.

Deleted: successfully

Deleted: ies



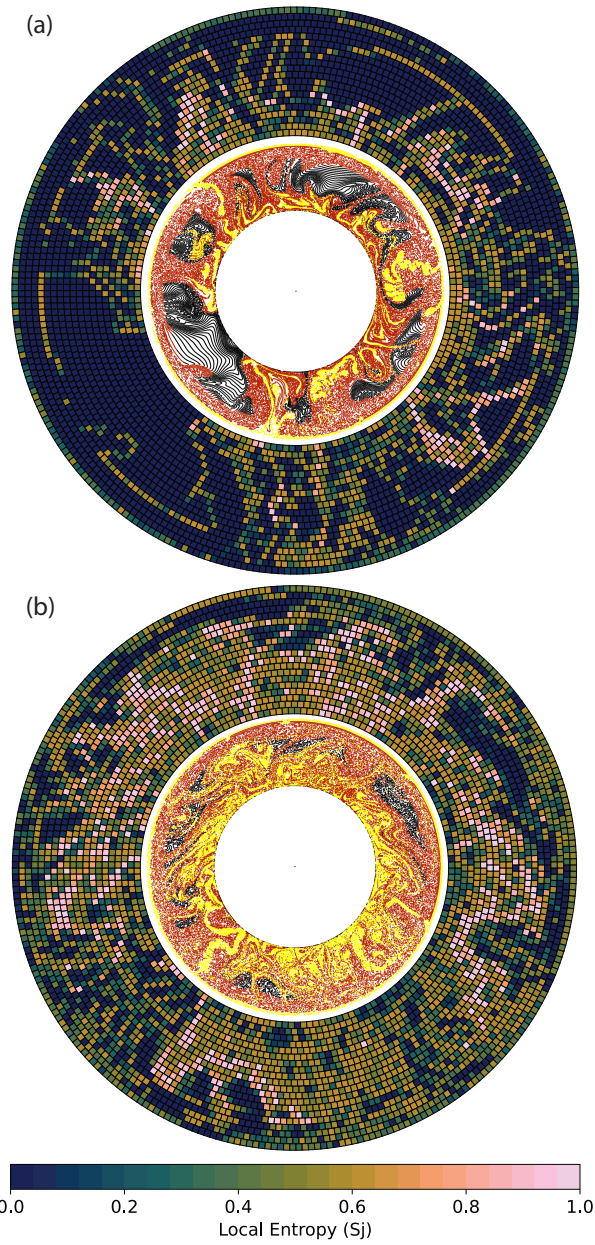


Figure 7 - Local Entropy  $S_j$  with a 20x160 resolution (outer annulus) and particle distribution (inner annulus) for dynamic compositions after 1000 Ma of simulated convection. Lower mantle (black), upper mantle (red) and lithosphere (yellow) compositions can change over time as function of depth. a) model R and b) model P with more vigorous convection of van der Wiel et al., (2023) as described in section 3.4.

Deleted:

#### 400 4. Outlook and conclusion

401 In this paper, we explore how configurational entropy may be applied to mantle  
402 convection models to quantify the degree of mechanical mixing, both on a local and global  
403 scale. Our results illustrate that entropy provides a way to track or map compositional  
404 heterogeneity over time using tracers or particles, which are commonly available in  
405 geodynamical models. Depending on the complexity of numerical models, any information  
406 that is stored on these tracers can be used to differentiate between ‘compositions’ used in  
407 the entropy calculations. The mantle convection models that we used to illustrate the use of  
408 configurational entropy were designed as numerical experiments to evaluate whether slab  
409 sinking rates scale with the vigor of mantle convection and mixing and did not aim to make a  
410 direct comparison between model and the real Earth. A direct comparison between  
411 configurational entropy and other measures used to quantify mixing, like the Lyapunov  
412 exponents (or time), is beyond the scope of this work. We see two arguments in favor of  
413 configurational entropy for specific uses: 1) its measurement does not require an integration  
414 over time thereby providing instant values for local and global entropy and 2) its flexibility,  
415 since the spatial distribution of any field carried by the particles, passive or active, such as  
416 chemical composition, water-content, reached depth or temperature, can be quantified.

417 For models that do make comparisons with the Earth, i.e. kinematically constrained  
418 by reconstructed plate motions and aiming to resemble Earth-like features (e.g., (Bull et al.,  
419 2014; Coltice & Shephard, 2018; Faccenna et al., 2013; Flament et al., 2022; Li et al., 2023;  
420 Lin et al., 2022) configurational entropy may serve as a means to quantify and map the  
421 degree of mixing of varying compositions, and hence to determine average cell composition,  
422 on a local, regional or a global scale. In such models the Lyapunov time would be useful to

Deleted: However, for

Deleted: ¶  
→

quantify the deformation, or stretching, in the overall mantle (e.g., (Coltice, 2005; van Keken & Zhong, 1999) or quantifying uncertainties in twin-experiments (e.g., (Bello et al., 2014; Bocher et al., 2016)).

On a global scale, such models (if run for 2-4 Ga) would for instance be able to track volumes of material that have remained in the lower mantle during the evolution of Earth (Fig. 7). These volumes are of interest, because they could explain the geochemical detection of enigmatic primordial mantle, and feature in numerical models as the proposed bridgmanite-enriched ancient mantle structures (BEAMS) of (Ballmer et al., 2017), or surviving in the slab graveyard (Jones et al., 2021), or perhaps in LLSVPs or ULVZs (Deschamps et al., 2012; Flament et al., 2022; McNamara, 2019; Vilella et al., 2021). In addition, the use of entropy calculations may show how subducted lithosphere may become stored in the mantle and to what degree original depleted and enriched crust, and slab material mix with upper and lower mantle rock. Particularly, dynamically changing compositions would benefit such studies, and in more sophisticated models that include geochemical evolution (e.g., (Dannberg & Gassmüller, 2018; Gülcher et al., 2021), geochemical reservoirs can be quantified with configurational entropy.

At smaller scales, entropy in mantle modeling is useful to track mixing at the scale of a single subducting plate interacting with a mantle wedge, or a plume rising from the CMB. This may be done based on location solely ( $S_{pd}$ ), to track the dispersal of an initial cloud of tracers in a slab or at the base of a plume (Naliboff & Kellogg, 2007), but also with the use of composition through  $S_j$  and  $S$ . For instance, it may quantify how different compositions of material from the lowermost mantle are entrained by a plume and how material entrained by that plume is mixed during its upward motion (e.g., (Dannberg & Gassmüller, 2018). For instance, how material is mixed in the partially melting plume head, or in the partially

Formatted: Indent: First line: 1.27 cm

450 melting upper mantle below a ridge, mixing on the scale of a magma chamber may also be  
451 mapped using configurational entropy, see (Perugini et al., 2015).

452       However, it may not yet be possible to numerically represent 3D mixing and motion  
453 processes on all the scales illustrated above. In the end, the dynamics driving mantle  
454 convection may force slow consumption and mixing away of primordial mantle by producing  
455 lithosphere and plumes and mixing the geochemically segregated remains of these back into  
456 the mantle. These processes lie at the basis for the widely recognized but still enigmatic  
457 geochemical reservoirs that are thought to reside in the lower mantle such as those of  
458 recycled continental crust (EM1, EM2), recycled oceanic crust (HIMU) (Yan et al., 2020),  
459 recycled depleted lithospheric mantle (Stracke et al., 2019), and remaining primordial  
460 mantle (Ballmer et al., 2017; Gülcher et al., 2020; Jackson et al., 2017). These processes also  
461 culminate in the seismologically imaged mantle volumes of higher and lower seismic  
462 velocity, or seismic attenuation, but the widely different scales at which geochemical and  
463 seismological observations are made poses a problem to link such observations. Numerical  
464 models may bridge these scales and eventually use our planets plate tectonic evolution to  
465 predict the geochemical reservoirs as tapped by volcanoes, and mantle structure as imaged  
466 by seismology. The configurational entropy in this paper may be helpful to quantitatively  
467 determine where numerical models may successfully predict these seismological and  
468 geochemical features.

## 469 Appendix A

470 We here recall the equations of the manuscript and show the equations for normalization. [Where](#)

471 [n<sub>c,j</sub> is the number of particles per composition c in a cell j and N<sub>c</sub> is the total number of c-](#)  
472 [particles divided by the number of cells M. C represents the number of compositions used.](#)

$$473 \quad \rho_{c,j} = \frac{n_{c,j}}{N_c} \quad (1)$$

$$474 \quad P_{j,c} = \frac{\rho_{c,j}}{\sum_{c=1}^C \rho_{c,j}} \quad (2)$$

$$475 \quad P_j = \frac{\sum_{c=1}^C \rho_{c,j}}{\sum_{j=1}^M \sum_{c=1}^C \rho_{c,j}} \quad (3)$$

$$476 \quad S_{pd} = -\sum_{j=1}^M P_j \ln P_j \quad (4)$$

$$477 \quad S_j = -\sum_{c=1}^C P_{j,c} \ln P_{j,c} \quad (5)$$

$$478 \quad S = \sum_{j=1}^M P_j S_j \quad (6)$$

$$479 \quad S_{pd \text{ normalized}} = \frac{S_{pd}}{\ln M} \quad (7)$$

$$480 \quad S_j \text{ normalized} = \frac{S_j}{\ln C} \quad (8)$$

$$481 \quad S_{\text{normalized}} = \frac{S}{\ln C} \quad (9)$$

482

483

484 Four examples are given below, each with different distributions of particles and  
485 compositions in a small rectangular grid of 4 cells. We use these four examples to illustrate  
486 how the configurational entropy is affected by certain distributions. The background of the  
487 cells is colored according to S<sub>j</sub> in grayscale, from 0 (black) to 1 (white) and the tracers shown  
488 are randomly given a position in the cell appointed to them.

### Example 1 – equal distribution, fully mixed

We start with a uniform distribution of particles with completely mixed compositions in each cell. The number of expected particles per composition per cell ( $N_c$ ) is equal to the sum of the number of particles in that cell, this also reflected in vector  $P_j$  which is equal for all cells – and therefore  $S_{pd}$  is equal to 1 (after normalization) indicating a uniform distribution. The local entropy  $S_j$  per cell is defined through  $P_{j,c}$  which is equally distributed and equal to the normalization. Therefore, it indicates perfect mixing for all four cells. The global entropy combines  $P_j$  and  $S_j$  and is therefore equal to the endmember, which is 1.

$$n_{c,j} = \begin{pmatrix} 3 & 3 & 3 & 3 \\ 3 & 3 & 3 & 3 \end{pmatrix}$$

$$N_c = \begin{pmatrix} 3 \\ 3 \end{pmatrix}$$

$$\rho_{c,j} = \begin{pmatrix} 1 & 1 & 1 & 1 \\ 1 & 1 & 1 & 1 \end{pmatrix}$$

$$P_{j,c} = \begin{pmatrix} 1/2 & 1/2 & 1/2 & 1/2 \\ 1/2 & 1/2 & 1/2 & 1/2 \end{pmatrix}$$

$$P_j = (1/4 \ 1/4 \ 1/4 \ 1/4)$$

$$S_{pd} = 1.38629$$

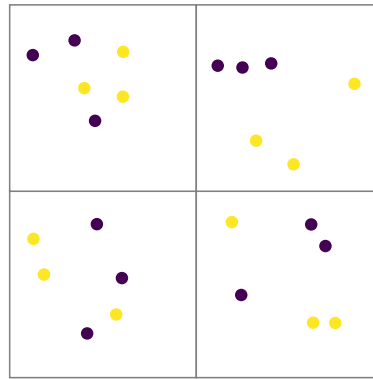
$$S_j = (0.693 \ 0.693 \ 0.693 \ 0.693)$$

$$S = 0.69314$$

$$S_{pd \text{ normalized}} = \frac{1.38629}{\ln 4} = 1$$

$$S_j \text{ normalized} = (1 \ 1 \ 1 \ 1)$$

$$S_{\text{normalized}} = \frac{0.69314}{\ln 2} = 1$$



### Example 2 – equal distribution, no mixing

The spatial distribution of particles is the same as in example 1 but compositions are not mixed, so  $S_{pd}$  is still 1.  $P_{j,c}$  is either one or zero per composition which both will lead to a zero for the local entropy which is therefore 0 for all four cells. As this local entropy feeds into the global entropy  $S$ , that is also 0.

$$n_{c,j} = \begin{pmatrix} 0 & 0 & 4 & 4 \\ 4 & 4 & 0 & 0 \end{pmatrix}$$

$$N_c = \begin{pmatrix} 2 \\ 2 \end{pmatrix}$$

$$\rho_{c,j} = \begin{pmatrix} 0 & 0 & 2 & 2 \\ 2 & 2 & 0 & 0 \end{pmatrix}$$

$$P_{j,c} = \begin{pmatrix} 0 & 0 & 1 & 1 \\ 1 & 1 & 0 & 0 \end{pmatrix}$$

$$P_j = (1/4 \ 1/4 \ 1/4 \ 1/4)$$

$$S_{pd} = 1.38629$$

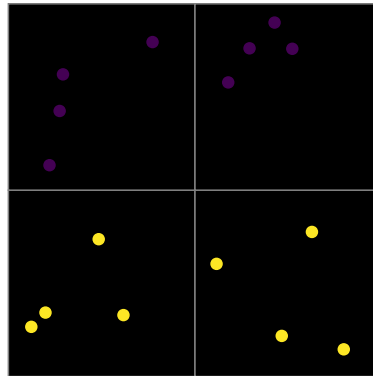
$$S_j = (0 \ 0 \ 0 \ 0)$$

$$S = 0$$

$$S_{pd \text{ normalized}} = \frac{1.38629}{\ln 4} = 1$$

$$S_j \text{ normalized} = (0 \ 0 \ 0 \ 0)$$

$$S_{\text{normalized}} = \frac{0}{\ln 2} = 0$$



### Example 3 – random example with 3 compositions

The distribution is ideally mixed as the expected number of particles in each cell is 3.5.  $P_j$  is therefore not the same in each cell, but close to that.  $S_{pd}$  is therefore close to 1 in this example. The compositions are not equally distributed, the top left cell is close to the expected distribution ( $N_c$ ) and therefore has a local entropy close to 1 (after normalization by  $\ln(3)$ ). The bottom cells are equally far off expected values (1.5 off for purple, and 1 for the other colors) and have therefore the same  $S_j$ . As three cells have local entropy of about 0.5, but distributions are somewhat equal, the global normalized entropy is 0.678 – ~~this~~ reflects the weighted average of  $S_j$  which is the global entropy.

Deleted: which

Deleted: is

$$n_{c,j} = \begin{pmatrix} 3 & 0 & 2 & 1 \\ 1 & 2 & 1 & 0 \\ 0 & 1 & 1 & 2 \\ 1.5 & & & \end{pmatrix}$$

$$N_c = \begin{pmatrix} 1 \\ 1 \\ 1 \end{pmatrix}$$

$$\rho_{c,j} = \begin{pmatrix} 2 & 0 & 4/3 & 2/3 \\ 1 & 2 & 1 & 0 \\ 0 & 1 & 1 & 2 \end{pmatrix}$$

$$P_{j,c} = \begin{pmatrix} 2/3 & 0 & 4/10 & 1/4 \\ 1/3 & 2/3 & 3/10 & 0 \\ 0 & 1/3 & 3/10 & 3/4 \end{pmatrix}$$

$$P_j = \begin{pmatrix} 1/4 & 1/4 & 5/18 & 2/9 \end{pmatrix}$$

$$S_{pd} = 1.3832$$

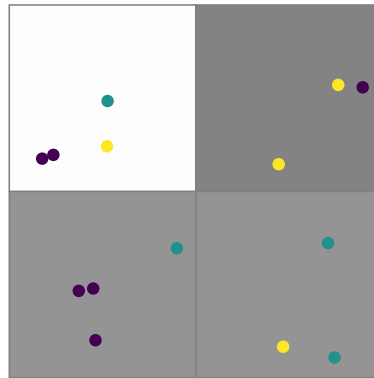
$$S_j = (0.6365 \ 0.6365 \ 1.0888 \ 0.5623)$$

$$S = 0.74569$$

$$S_{pd \text{ normalized}} = \frac{1.38629}{\ln 4} = 0.99777$$

$$S_j \text{ normalized} = (0.5794 \ 0.5794 \ 0.9912 \ 0.5119)$$

$$S_{\text{normalized}} = \frac{0.74569}{\ln 3} = 0.67876$$



#### Example 4 – no equal distribution

This last case showcases an uneven particle distribution, with an expected number of particles of 16.75 (sum  $N_c$ ) that is not recovered in any cell. The vector  $P_j$  is therefore not balanced and  $S_{pd \text{ normalized}}$  is 0.689, indicating an imperfect particle distribution. The top left is obviously unmixed with  $S_j = 0$ . The bottom cells have the same ratio of compositions and therefore a similar high  $S_j$  as the 50/50 compositional ratio is not too far off the ideal ratio. The bottom cells contribute significantly to the global entropy  $S$  and the top left cell has a sizable weighing factor ( $P_3 = 0.238$ ) but as its  $S_j = 0$  it does therefore not contribute to the total entropy.

$$n_{c,j} = \begin{pmatrix} 20 & 1 & 20 & 1 \\ 20 & 1 & 0 & 4 \end{pmatrix}$$

$$N_c = \begin{pmatrix} 10.5 \\ 6.25 \end{pmatrix}$$

$$\rho_{c,j} = \begin{pmatrix} 1.9 & 0.095 & 1.905 & 0.095 \\ 3.2 & 0.16 & 0 & 0.64 \end{pmatrix}$$

$$P_{j,c} = \begin{pmatrix} 0.373 & 0.373 & 1 & 0.129 \\ 0.627 & 0.627 & 0 & 0.871 \end{pmatrix}$$

$$P_j = (0.638 \ 0.0319 \ 0.2381 \ 0.0919)$$

$$S_{pd} = 0.9576$$

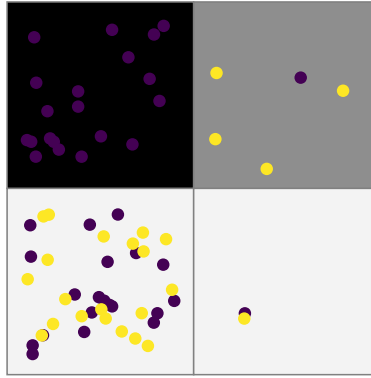
$$S_j = (0.66 \ 0.66 \ 0 \ 0.385)$$

$$S = 0.478$$

$$S_{pd \text{ normalized}} = \frac{0.9576}{\ln 4} = 0.6907$$

$$S_j \text{ normalized} = (0.953 \ 0.953 \ 0 \ 0.556)$$

$$S_{\text{normalized}} = \frac{0.478}{\ln 2} = 0.689$$





576 **Code availability**

577 The code that is used to create the appendix which calculates all the appropriate values can be found  
578 online at:

579 [https://github.com/cedrict/fieldstone/blob/master/python\\_codes/fieldstone\\_137/ministone.py](https://github.com/cedrict/fieldstone/blob/master/python_codes/fieldstone_137/ministone.py)

580

581 **Data availability**

582 The data used to make the figures are available on Zenodo (<https://zenodo.org/records/10077983>)

583

584 **CRediT authorship contribution statement**

585 **EvdW:** Conceptualization, Methodology, Investigation, Writing – Original draft, Visualization **CT:**

586 Methodology, Writing – Review & Editing **DJJvH:** Supervision, Writing – Review & Editing

587

588 **Competing interests**

589 The authors declare that they have no conflict of interest.

590

591 **Acknowledgements**

592 We thank W. Spakman for discussions. EvdW and DJJvH acknowledge the support by the Netherlands

593 Organisation for Scientific Research through NWO Vici Grant 865.17.001.

## References

- Ballmer, M. D., Houser, C., Hernlund, J. W., Wentzcovitch, R. M., & Hirose, K. (2017). Persistence of strong silica-enriched domains in the Earth's lower mantle. *Nature Geoscience*, 10(3), 236-240. <https://doi.org/10.1038/NGEO2898>
- Bello, L., Coltice, N., Rolf, T., & Tackley, P. J. (2014). On the predictability limit of convection models of the Earth's mantle. *Geochemistry, Geophysics, Geosystems*, 15(6), 2319-2328.
- Bocher, M., Coltice, N., Fournier, A., & Tackley, P. J. (2016). A sequential data assimilation approach for the joint reconstruction of mantle convection and surface tectonics. *Geophysical Journal International*, 204(1), 200-214.
- Bower, D. J., Gurnis, M., & Flament, N. (2015). Assimilating lithosphere and slab history in 4-D Earth models. *Physics of the Earth and planetary interiors*, 238, 8-22. <https://doi.org/10.1016/j.pepi.2014.10.013>
- Bull, A. L., Domeier, M., & Torsvik, T. H. (2014). The effect of plate motion history on the longevity of deep mantle heterogeneities. *Earth and Planetary Science Letters*, 401, 172-182. <https://doi.org/10.1016/j.epsl.2014.06.008>
- Camesasca, M., Kaufman, M., & Manas-Zloczower, I. (2006). Quantifying fluid mixing with the Shannon entropy. *Macromolecular theory and simulations*, 15(8), 595-607. <https://doi.org/10.1002/mats.200600037>
- Christensen, U. (1989). Mixing by time-dependent convection. *Earth and Planetary Science Letters*, 95(3-4), 382-394.
- Colli, L., Bunge, H. P., & Schuberth, B. S. (2015). On retrodictions of global mantle flow with assimilated surface velocities. *Geophysical Research Letters*, 42(20), 8341-8348.
- Coltice, N. (2005). The role of convective mixing in degassing the Earth's mantle. *Earth and Planetary Science Letters*, 234(1-2), 15-25.
- Coltice, N., & Schmalzl, J. (2006). Mixing times in the mantle of the early Earth derived from 2-D and 3-D numerical simulations of convection. *Geophysical Research Letters*, 33(23). <https://doi.org/10.1029/2006GL027707>
- Coltice, N., & Shephard, G. E. (2018). Tectonic predictions with mantle convection models. *Geophysical Journal International*, 213(1), 16-29. <https://doi.org/10.1093/gji/ggx531>
- Dannberg, J., & Gassmüller, R. (2018). Chemical trends in ocean islands explained by plume-slab interaction. *Proceedings of the National Academy of Sciences*, 115(17), 4351-4356. <https://doi.org/10.1073/pnas.1714125115>

639 Deschamps, F., Cobden, L., & Tackley, P. J. (2012). The primitive nature of large low shear-  
 640 wave velocity provinces. *Earth and Planetary Science Letters*, 349, 198-208.  
 641 <https://doi.org/10.1016/j.epsl.2012.07.012>  
 642  
 643 Domeier, M., & Torsvik, T. H. (2014). Plate tectonics in the late Paleozoic. *Geoscience*  
 644 *Frontiers*, 5(3), 303-350. <https://doi.org/10.1016/j.gsf.2014.01.002>  
 645  
 646 Doucet, L. S., Li, Z.-X., Gamal El Dien, H., Pourteau, A., Murphy, J. B., Collins, W. J., Mattielli,  
 647 N., Olierook, H. K., Spencer, C. J., & Mitchell, R. N. (2020). Distinct formation history  
 648 for deep-mantle domains reflected in geochemical differences. *Nature Geoscience*,  
 649 13(7), 511-515. <https://doi.org/10.1038/s41561-020-0599-9>  
 650  
 651 Dupré, B., & Allègre, C. J. (1983). Pb–Sr isotope variation in Indian Ocean basalts and mixing  
 652 phenomena. *Nature*, 303(5913), 142-146. <https://doi.org/10.1038/303142a0>  
 653  
 654 Faccenna, C., Becker, T. W., Conrad, C. P., & Husson, L. (2013). Mountain building and mantle  
 655 dynamics. *Tectonics*, 32(1), 80-93. <https://doi.org/10.1029/2012TC003176>  
 656  
 657 Farnetani, C. G., Legras, B., & Tackley, P. J. (2002). Mixing and deformations in mantle  
 658 plumes. *Earth and Planetary Science Letters*, 196(1-2), 1-15.  
 659  
 660 Farnetani, C. G., & Samuel, H. (2003). Lagrangian structures and stirring in the Earth's  
 661 mantle. *Earth and Planetary Science Letters*, 206(3-4), 335-348.  
 662  
 663 Ferrachat, S., & Ricard, Y. (1998). Regular vs. chaotic mantle mixing. *Earth and Planetary*  
 664 *Science Letters*, 155(1-2), 75-86.  
 665  
 666 Ferrachat, S., & Ricard, Y. (2001). Mixing properties in the Earth's mantle: Effects of the  
 667 viscosity stratification and of oceanic crust segregation. *Geochemistry, Geophysics,*  
 668 *Geosystems*, 2(4).  
 669  
 670 Flament, N., Bodur, Ö. F., Williams, S. E., & Merdith, A. S. (2022). Assembly of the basal  
 671 mantle structure beneath Africa. *Nature*, 603(7903), 846-851.  
 672 <https://doi.org/10.1038/s41586-022-04538-y>  
 673  
 674 Garnero, E. J., McNamara, A. K., & Shim, S.-H. (2016). Continent-sized anomalous zones with  
 675 low seismic velocity at the base of Earth's mantle. *Nature Geoscience*, 9(7), 481-489.  
 676 <https://doi.org/10.1038/NGEO2733>  
 677  
 678 Gazel, E., Trela, J., Bizimis, M., Sobolev, A., Batanova, V., Class, C., & Jicha, B. (2018). Long-  
 679 lived source heterogeneities in the Galapagos mantle plume. *Geochemistry,*  
 680 *Geophysics, Geosystems*, 19(8), 2764-2779. <https://doi.org/10.1029/2017GC007338>  
 681  
 682 Gerya, T. (2014). Precambrian geodynamics: concepts and models. *Gondwana Research*,  
 683 25(2), 442-463. <https://doi.org/10.1016/j.gr.2012.11.008>  
 684

685 Goltz, C., & Böse, M. (2002). Configurational entropy of critical earthquake populations.  
686 *Geophysical Research Letters*, 29(20), 51-51-51-54.  
687 <https://doi.org/10.1029/2002GL015540>  
688  
689 Gottschaldt, K.-D., Walzer, U., Hendel, R., Stegman, D. R., Baumgardner, J., & Mühlhaus, H.-B.  
690 (2006). Stirring in 3-d spherical models of convection in the Earth's mantle.  
691 *Philosophical Magazine*, 86(21-22), 3175-3204.  
692  
693 Gülcher, A. J., Gebhardt, D. J., Ballmer, M. D., & Tackley, P. J. (2020). Variable dynamic styles  
694 of primordial heterogeneity preservation in the Earth's lower mantle. *Earth and*  
695 *Planetary Science Letters*, 536, 116160. <https://doi.org/10.1016/j.epsl.2020.116160>  
696  
697 Gülcher, A. J. P., Ballmer, M. D., & Tackley, P. J. (2021). Coupled dynamics and evolution of  
698 primordial and recycled heterogeneity in Earth's lower mantle. *Solid Earth*, 12(9),  
699 2087-2107. <https://doi.org/10.5194/se-12-2087-2021>  
700  
701 Gurnis, M., & Davies, G. F. (1986a). The effect of depth-dependent viscosity on convective  
702 mixing in the mantle and the possible survival of primitive mantle. *Geophysical*  
703 *Research Letters*, 13(6), 541-544.  
704  
705 Gurnis, M., & Davies, G. F. (1986b). Mixing in numerical models of mantle convection  
706 incorporating plate kinematics. *Journal of Geophysical Research: Solid Earth*, 91(B6),  
707 6375-6395.  
708  
709 Hart, S. R. (1984). A large-scale isotope anomaly in the Southern Hemisphere mantle.  
710 *Nature*, 309(5971), 753-757. <https://doi.org/10.1038/309753a0>  
711  
712 Heister, T., Dannberg, J., Gassmöller, R., & Bangerth, W. (2017). High accuracy mantle  
713 convection simulation through modern numerical methods – II: realistic models and  
714 problems. *Geophysical Journal International*, 210(2), 833-851.  
715 <https://doi.org/10.1093/gji/ggx195>  
716  
717 Hoernle, K., Werner, R., Morgan, J. P., Garbe-Schönberg, D., Bryce, J., & Mrazek, J. (2000).  
718 Existence of complex spatial zonation in the Galápagos plume. *Geology*, 28(5), 435-  
719 438. [https://doi.org/10.1130/0091-7613\(2000\)28<435:EOCSZI>2.0.CO;2](https://doi.org/10.1130/0091-7613(2000)28<435:EOCSZI>2.0.CO;2)  
720  
721 Hoffman, N., & McKenzie, D. (1985). The destruction of geochemical heterogeneities by  
722 differential fluid motions during mantle convection. *Geophysical Journal*  
723 *International*, 82(2), 163-206.  
724  
725 Homrighausen, S., Hoernle, K., Hauff, F., Hoyer, P. A., Haase, K. M., Geissler, W. H., &  
726 Geldmacher, J. (2023). Evidence for compositionally distinct upper mantle plumelets  
727 since the early history of the Tristan-Gough hotspot. *Nature communications*, 14(1),  
728 3908. <https://doi.org/10.1038/s41467-023-39585-0>  
729

730 Hunt, D., & Kellogg, L. (2001). Quantifying mixing and age variations of heterogeneities in  
731 models of mantle convection: Role of depth-dependent viscosity. *Journal of*  
732 *Geophysical Research: Solid Earth*, 106(B4), 6747-6759.

733

734 Jackson, M., Becker, T., & Konter, J. (2018). Evidence for a deep mantle source for EM and  
735 HIMU domains from integrated geochemical and geophysical constraints. *Earth and*  
736 *Planetary Science Letters*, 484, 154-167. <https://doi.org/10.1016/j.epsl.2017.11.052>

737

738 Jackson, M., Konter, J., & Becker, T. (2017). Primordial helium entrained by the hottest  
739 mantle plumes. *Nature*, 542(7641), 340-343. <https://doi.org/10.1038/nature21023>

740

741 Jackson, M., & Macdonald, F. (2022). Hemispheric geochemical dichotomy of the mantle is a  
742 legacy of austral supercontinent assembly and onset of deep continental crust  
743 subduction. *AGU Advances*, 3(6), e2022AV000664.  
744 <https://doi.org/10.1029/2022AV000664>

745

746 Jones, T. D., Sime, N., & van Keken, P. (2021). Burying Earth's primitive mantle in the slab  
747 graveyard. *Geochemistry, Geophysics, Geosystems*, 22(3), e2020GC009396.  
748 <https://doi.org/10.1029/2020GC009396>

749

750 Kellogg, L., & Turcotte, D. (1990). Mixing and the distribution of heterogeneities in a  
751 chaotically convecting mantle. *Journal of Geophysical Research: Solid Earth*, 95(B1),  
752 421-432. <https://doi.org/10.1029/JB095iB01p00421>

753

754 Kellogg, L. H. (1993). Chaotic mixing in the Earth's mantle. In *Advances in geophysics* (Vol. 34,  
755 pp. 1-33). Elsevier.

756

757 Koelemeijer, P., Deuss, A., & Ritsema, J. (2017). Density structure of Earth's lowermost  
758 mantle from Stoneley mode splitting observations. *Nature communications*, 8(1), 1-  
759 10. <https://doi.org/10.1038/ncomms15241>

760

761 Li, Y., Liu, L., Peng, D., Dong, H., & Li, S. (2023). Evaluating tomotectonic plate reconstructions  
762 using geodynamic models with data assimilation, the case for North America. *Earth-*  
763 *Science Reviews*, 104518. <https://doi.org/10.1016/j.earscirev.2023.104518>

764

765 Lin, Y. A., Colli, L., & Wu, J. (2022). NW Pacific-Panthalassa intra-oceanic subduction during  
766 Mesozoic times from mantle convection and geoid models. *Geochemistry,*  
767 *Geophysics, Geosystems*, e2022GC010514. <https://doi.org/10.1029/2022GC010514>

768

769 McNamara, A. K. (2019). A review of large low shear velocity provinces and ultra low velocity  
770 zones. *Tectonophysics*, 760, 199-220. <https://doi.org/10.1016/j.tecto.2018.04.015>

771

772 Merdith, A. S., Williams, S. E., Collins, A. S., Tetley, M. G., Mulder, J. A., Blades, M. L., Young,  
773 A., Armistead, S. E., Cannon, J., & Zahirovic, S. (2021). Extending full-plate tectonic  
774 models into deep time: Linking the Neoproterozoic and the Phanerozoic. *Earth-*  
775 *Science Reviews*, 214, 103477. <https://doi.org/10.1016/j.earscirev.2020.103477>

776

- Naliboff, J. B., & Kellogg, L. H. (2007). Can large increases in viscosity and thermal conductivity preserve large-scale heterogeneity in the mantle? *Physics of the Earth and planetary interiors*, 161(1-2), 86-102. <https://doi.org/10.1016/j.pepi.2007.01.009>
- Olson, P., Yuen, D. A., & Balsiger, D. (1984a). Convective mixing and the fine structure of mantle heterogeneity. *Physics of the Earth and planetary interiors*, 36(3-4), 291-304.
- Olson, P., Yuen, D. A., & Balsiger, D. (1984b). Mixing of passive heterogeneities by mantle convection. *Journal of Geophysical Research: Solid Earth*, 89(B1), 425-436.
- Perugini, D., De Campos, C., Petrelli, M., Morgavi, D., Vetere, F. P., & Dingwell, D. (2015). Quantifying magma mixing with the Shannon entropy: Application to simulations and experiments. *Lithos*, 236, 299-310. <https://doi.org/10.1016/j.lithos.2015.09.008>
- Richter, F. M., Daly, S. F., & Nataf, H.-C. (1982). A parameterized model for the evolution of isotopic heterogeneities in a convecting system. *Earth and Planetary Science Letters*, 60(2), 178-194.
- Ritsema, J., Deuss, A., Van Heijst, H., & Woodhouse, J. (2011). S40RTS: a degree-40 shear-velocity model for the mantle from new Rayleigh wave dispersion, teleseismic traveltimes and normal-mode splitting function measurements. *Geophysical Journal International*, 184(3), 1223-1236. <https://doi.org/10.1111/j.1365-246X.2010.04884.x>
- Ritsema, J., & Lekić, V. (2020). Heterogeneity of seismic wave velocity in Earth's mantle. *Annual Review of Earth and Planetary Sciences*, 48, 377-401. <https://doi.org/10.1146/annurev-earth-082119-065909>
- Samuel, H., Aleksandrov, V., & Deo, B. (2011). The effect of continents on mantle convective stirring. *Geophysical Research Letters*, 38(4).
- Schmalzl, J., Houseman, G., & Hansen, U. (1996). Mixing in vigorous, time-dependent three-dimensional convection and application to Earth's mantle. *Journal of Geophysical Research: Solid Earth*, 101(B10), 21847-21858.
- Shannon, C. E. (1948). A mathematical theory of communication. *The Bell system technical journal*, 27(3), 379-423. <https://doi.org/10.1002/j.1538-7305.1948.tb01338.x>
- Stegman, D. R., Richards, M. A., & Baumgardner, J. R. (2002). Effects of depth-dependent viscosity and plate motions on maintaining a relatively uniform mid-ocean ridge basalt reservoir in whole mantle flow. *Journal of Geophysical Research: Solid Earth*, 107(B6), ETG 5-1-ETG 5-8.
- Stracke, A., Genske, F., Berndt, J., & Koornneef, J. M. (2019). Ubiquitous ultra-depleted domains in Earth's mantle. *Nature Geoscience*, 12(10), 851-855. <https://doi.org/10.1038/s41561-019-0446-z>

823 Tackley, P. J., & Xie, S. (2002). The thermochemical structure and evolution of Earth's mantle:  
824 constraints and numerical models. *Philosophical Transactions of the Royal Society of*  
825 *London. Series A: Mathematical, Physical and Engineering Sciences*, 360(1800), 2593-  
826 2609.

827

828 Ten, A. A., Podladchikov, Y. Y., Yuen, D. A., Larsen, T. B., & Malevsky, A. V. (1998). Comparison  
829 of mixing properties in convection with the Particle-Line Method. *Geophysical*  
830 *Research Letters*, 25(16), 3205-3208.

831

832 Thieulot, C. (2018). Ghost: Geoscientific hollow sphere tessellation. *Solid Earth*, 9(5), 1169-  
833 1177. <https://doi.org/10.5194/se-9-1169-2018>

834

835 Thomas, B., Samuel, H., Farnetani, C., Aubert, J., & Chauvel, C. (2024). Mixing time of  
836 heterogeneities in a buoyancy-dominated magma ocean. *Geophysical Journal*  
837 *International*, 236(2), 764-777.

838

839 van der Meer, D. G., van Hinsbergen, D. J. J., & Spakman, W. (2018). Atlas of the underworld:  
840 Slab remnants in the mantle, their sinking history, and a new outlook on lower  
841 mantle viscosity. *Tectonophysics*, 723, 309-448.  
842 <https://doi.org/10.1016/j.tecto.2017.10.004>

843

844 van der Wiel, E., van Hinsbergen, D. J., Thieulot, C., & Spakman, W. (2024). Linking rates of  
845 slab sinking to long-term lower mantle flow and mixing. *Earth and Planetary Science*  
846 *Letters*, 625, 118471. <https://doi.org/10.1016/j.epsl.2023.118471>

847

848 van Keken, P., & Zhong, S. (1999). Mixing in a 3D spherical model of present-day mantle  
849 convection. *Earth and Planetary Science Letters*, 171(4), 533-547.

850

851 van Keken, P. E., Ballentine, C. J., & Hauri, E. H. (2003). Convective mixing in the Earth's  
852 mantle. *Treatise on geochemistry*, 2, 1-21.

853

854 Vilella, K., Bodin, T., Boukaré, C.-E., Deschamps, F., Badro, J., Ballmer, M. D., & Li, Y. (2021).  
855 Constraints on the composition and temperature of LLSVPs from seismic properties  
856 of lower mantle minerals. *Earth and Planetary Science Letters*, 554, 116685.  
857 <https://doi.org/10.1016/j.epsl.2020.116685>

858

859 Weis, D., Garcia, M. O., Rhodes, J. M., Jellinek, M., & Scoates, J. S. (2011). Role of the deep  
860 mantle in generating the compositional asymmetry of the Hawaiian mantle plume.  
861 *Nature Geoscience*, 4(12), 831-838. <https://doi.org/10.1038/ngeo1328>

862

863 Wellmann, J. F., & Regenauer-Lieb, K. (2012). Uncertainties have a meaning: Information  
864 entropy as a quality measure for 3-D geological models. *Tectonophysics*, 526, 207-  
865 216. <https://doi.org/10.1016/j.tecto.2011.05.001>

866

867 Wichmann, D., Delandmeter, P., Dijkstra, H. A., & van Sebille, E. (2019). Mixing of passive  
868 tracers at the ocean surface and its implications for plastic transport modelling.

869 *Environmental Research Communications*, 1(11), 115001.  
870 <https://doi.org/10.1088/2515-7620/ab4e77>  
871  
872 Yan, J., Ballmer, M. D., & Tackley, P. J. (2020). The evolution and distribution of recycled  
873 oceanic crust in the Earth's mantle: Insight from geodynamic models. *Earth and*  
874 *Planetary Science Letters*, 537, 116171. <https://doi.org/10.1016/j.epsl.2020.116171>  
875  
876